Analysis of Trends in Experimental Observables and Reconstruction of the Implosion Dynamics for Direct-Drive Cryogenic Targets on OMEGA

Introduction

This article describes a technique for identifying trends in performance degradation for inertial confinement fusion implosion experiments. It is based on reconstruction of the implosion core with a combination of low- and mid-mode asymmetries. This technique was applied to an ensemble of hydro-equivalent deuterium–tritium implosions on OMEGA that achieved inferred hot-spot pressures ≈56±7 Gbar (Ref. 1). All the experimental observables pertaining to the core could be reconstructed simultaneously with the same combination of low and mid modes. This suggests that in addition to low modes, which can cause a degradation of the stagnation pressure, mid modes are present that reduce the size of the neutron and x-ray–producing volume. The systematic analysis shows that asymmetries can cause an overestimation of the measured areal density in these implosions. It is also found that an improvement in implosion symmetry resulting from correction of either the systematic mid or low modes would result in an increase of the hot-spot pressure from 56 Gbar to ≈80 Gbar and could produce a burning plasma when the implosion core is extrapolated to an equivalent 1.9-MJ [National Ignition Facility (NIF)-scale] symmetric direct illumination.[2] This represents the current standing and the future potential of the 100-Gbar Direct-Drive Program on OMEGA.

Observation of repeatable data trends in the direct-drive experiments motivated the development of this analysis technique. Since the cause of performance degradation for direct-drive implosions is not yet fully identified, we use trends from simulations of the deceleration phase to infer the degradation mechanisms involved. It is known that Rayleigh–Taylor instability (RTI)–induced distortion of the implosion core is a likely cause of degradation; the asymmetries are categorized into low and mid modes, as in Ref. 3. For low modes ($\ell < 6$) the RTI wavelength is longer than the hot-spot radius, whereas for mid modes ($6 < \ell < 40$) the asymmetry wavelength is shorter than the hot-spot radius. It was also shown in Ref. 3 that the two types of asymmetries have different effects on the neutron-averaged quantities. This article focuses on trends in the experimental observables arising from asymmetries of the implosion core. The two types of asymmetries are used as the independent basis to approximately reproduce all of the experimental observables. Trends arising from an effective 1-D–like degradation, which may be caused by shortcomings in the physical models used in hydrocodes, are also documented in this article for future investigations of 1-D degradation.

It is important to emphasize that the experimental observables cannot be explained by using low or mid modes alone; the comprehensive analysis presented here shows that a combination of the two is necessary for the core reconstruction. The exact mode numbers degrading the experiments have not been determined in this article; other combinations of modes could also produce the observables. However, it is shown that in order to reconstruct all the observables simultaneously, the overall balance between the degradation by low modes and the degradation by mid modes must be preserved.

The following sections (1) summarize the experimental data used in the analysis; (2) describe the reconstruction technique and discuss the trends in the stagnation observables—the inferred pressure, volume, shape, temperature, areal density, neutron burnwidth, and bang time—arising from the various degradation mechanisms; and (3) present our conclusions along with an energy extrapolation of direct-drive implosions and future applications for this analysis technique.

Trends in Cryogenic Implosion Experiments

It has been shown by Regan *et al.*[1] that direct-drive cryogenic implosions on OMEGA have achieved hot-spot pressures exceeding 50 Gbar—a performance that surpassed all previous implosions on OMEGA. The implosion performance was estimated based on the experimental observables: neutron yield, areal density, ion temperature, hot-spot volume, and neutron burnwidth. The "50-Gbar" implosions used standardized pulse shapes (either a single-picket pulse or a triple-picket pulse) and standardized targets (shown in Fig. 154.1). The 1-D performance is estimated from simulations using the hydrodynamic code *LILAC*.[4] It must be noted that the laser deposition models in *LILAC* were optimized to reproduce in-flight observables

like laser-energy deposition and shell trajectory.[5,6] The estimated implosion adiabat for this design is $\alpha \approx 3.5$ to 4 [the adiabat is defined as the ratio of the hydrodynamic pressure (P) and the Fermi pressure of a degenerate electron gas (P_F), at the interface of the hot spot and shell at the time when the laser-driven shocks reach this interface, i.e., $\alpha \equiv P/P_F$]. This is considered to be a mid-adiabat implosion design, with an adiabat higher than the indirect-drive "high-foot" design.[7–9] The peak hot-spot pressure in 1-D is estimated to be ~100 Gbar, close to the ~120 Gbar required to demonstrate hydro-equivalent ignition (the hydro-equivalent scaling of the implosion core has been discussed in Refs. 1, 2, 10, and 11). Notice that the pressure required for ignition with 1.9-MJ direct illumination is lower than the 350 to 400 Gbar required for ignition with the indirect-drive approach and the same laser energy. This is because for direct drive the conversion efficiency of laser energy to kinetic energy of the imploding shell is much higher, therefore allowing the implosion of greater DT fuel mass (i.e., larger target radius), which results in longer confinement times (τ). Since the Lawson ignition condition scales as $P_{ign}\tau$, the pressure required for ignition (P_{ign}) is lower with respect to that required for indirect drive.

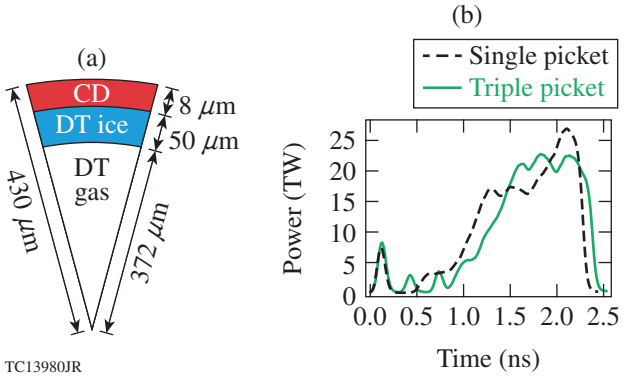

Figure 154.1
The pulse shapes and targets from the 50-Gbar implosions.[1]

Table 154.I lists the performance of several of these 50-Gbar implosions. The performance parameters are similar for all the shots. The neutron yields are ~4×10^{13}, at a yield degradation level $Y/Y_{1\text{-D}} \sim 0.3$, where $Y_{1\text{-D}}$ represents the post-shot 1-D

Table 154.I: The experimental observable and corresponding 1-D estimate from simulations [in brackets] for the ensemble of cryogenic implosions on OMEGA that produced ~50-Gbar pressure.

Shot	Y (×10^{13}) ±5%	X-ray $R_{17\%}$ (μm) ±0.5 μm	T_i (keV)[a] ±0.3 keV	ΔT_i (keV)	ρR (mg/cm^2)[b] ±31, ±19 mg/cm^2	Burnwidth (ps) ±6 ps	t_b–$t_{b,1\text{-D}}$ (ps) ±25 ps	P_{inf} (Gbar) ±7 Gbar
78959	4.39 [13.8]	21.3 [20.9]	3.63 [3.60]	0.54	213, 203 [232]	71 [54.1]	–16	52 [109]
78963	4.38 [16.3]	22.1 [19.8]	3.69 [3.74]	0.88	204, 208 [242]	67 [51.1]	–20	49 [126]
78967	3.76 [15.3]	21.4 [20.4]	3.65 [3.69]	0.85	179, 195 [238]	64 [51.1]	–46	50 [120]
78969	4.48 [14.1]	21.7 [21.4]	3.70 [3.66]	0.46	204, 197 [216]	59 [54.7]	–19	55 [104]
78971	3.77 [14.4]	22.1 [21.4]	3.69 [3.64]	1.06	220, 208 [222]	72 [20.9]	–27	44 [107]
77064	4.21 [12.5]	22.0 [20.4]	3.32 [3.48]	0.42	211, 191 [219]	62 [57.4]	–26	54 [108]
77066	4.11 [16.1]	21.9 [21.4]	3.18 [3.66]	0.57	221, 193 [228]	67 [52.9]	–20	56 [112]
77068	5.3 [17.0]	22.0 [22.0]	3.60 [3.82]	0.16	211, 194 [211]	66 [61.0]	–31	56 [97]
77070	4.02 [13.3]	20.3 [20.4]	3.40 [3.55]	0.23	220, 229 [239]	70 [52.6]	–11	56 [114]

[a]The ion temperatures were inferred using the instrument response function that was used prior to 2017. Currently an updated response function is being investigated that would result in temperatures that are ≈300 eV lower than stated and are within the experimental error.

[b]Both neutron time-of-flight and magnetic recoil spectrometer (second) measurements are listed.

simulation yield, calculated using *LILAC*. The hot-spot radii for all the shots are ~22 μm; they were estimated using time-resolved x-ray images.[12] The ion temperatures ($T_i \sim 3.5$ keV) are comparable to the temperatures from 1-D simulations, to within a 10% degradation level. The T_i's were measured using three different detectors—the chemical-vapor deposition (CVD) detector[13] and the 12-m and 15-m neutron time-of-flight (nTOF) detectors[14,15]—positioned along different implosion lines of sight; the minimum temperature is listed in Table 154.I. The variation in T_i measurement ΔT, which is the difference between the maximum and minimum measured temperatures, is considerable for a majority of the shots, ranging between 150 eV and 1.1 keV. It is observed that the measured areal densities are comparable to the 1-D estimates. The ρR is measured using the nTOF and magnetic recoil spectrometer (MRS)[16] detectors. The measured burnwidths are slightly longer than the 1-D estimate. The burnwidths are measured using the neutron temporal diagnostic (NTD).[17]

For direct-drive implosions on OMEGA, it is anticipated that the core is degraded by a combination of low and intermediate modes. Although the origin of the asymmetries is uncertain, low modes can arise from several factors, including long-wavelength target defects, target positioning, laser beam balance, and laser beam pointing.[18–20] In addition, the superposition of all 60 laser beams on OMEGA can produce overlapped intensity variations, which is expected to introduce intermediate-mode nonuniformities, similar to the mode ℓ = 10 in 2-D geometry. The cross-beam energy transfer (CBET) calculations by Edgell *et al.*,[21] shown in Fig. 154.2, represent the variation in laser-energy absorption at the target surface. When CBET is included, the nonuniformity is higher by 10×.

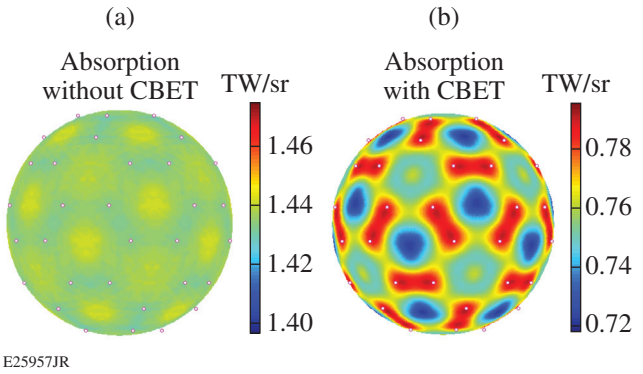

Figure 154.2
The laser power absorbed at the target surface is shown for calculations: (a) without considering cross-beam energy transfer (CBET) between the interacting laser beams and (b) with CBET.

These variations may be associated with the origin of mid-mode asymmetry in direct-drive implosions.

The Reconstruction Technique and Its Application

Unlike the conventional approach that involves full simulations of the implosions including nonuniformities from numerous sources, our technique focuses only on the final phase of an implosion. The final phase consists of the deceleration phase followed by stagnation and disassembly, which are critical in the production of fusion reaction neutrons detected by the nuclear diagnostics, and bremsstrahlung emission detected by the x-ray imaging diagnostics. Performance degradation results from a combination of nonuniformities: they are amplified by the RTI during the acceleration phase and can feed through to the inner surface, where they are further amplified during the deceleration phase by the RTI. Our technique is based on the multi-objective analysis of the degradation trends in the core observables and reconstruction of the implosion core.

The 2-D radiation–hydrodynamic code *DEC2D* is used to simulate the deceleration phase of implosions. The details of the code have been discussed in Ref. 10. Figure 154.3 provides an outline to our technique: the acceleration phase was simulated using *LILAC*;[4] it includes the laser drive with models for CBET[5] and nonlocal thermal transport.[6] The hydrodynamic profiles at the end of the laser pulse were used as initial conditions for the deceleration-phase simulations in 2-D. Initial perturbations for the deceleration-phase RTI were introduced at the interface of the shell and the hot spot through the angular variation of the velocity field.

Here we consider three categories of degradation: low-mode asymmetry, mid-mode asymmetry, and 1-D degradation. The low-mode trends are represented using mode 1 ("ℓ = 1"), mode 2 ("ℓ = 2"), and phase-reversed mode 2 ("ℓ = 2 *phase reversed*"); the RTI spike axis coincides with the simulation axis of symmetry for the former and is orthogonal for the latter. The mid-mode trends are represented using a mode-10 ("$\ell = 10^*$") and a multimode spectrum referred to as "*mid modes*." The $\ell = 10^*$ consists of a central mode 10 along with sideband modes 8 and 12 at 20% of central mode amplitude. The mid modes consist of a spectrum of modes given by $4 \le \ell \le 20$ at the same amplitude and a $1/\ell^2$ roll-off spectrum for higher modes $20 \le \ell \le 100$; the latter was motivated by the DT ice inner surface roughness spectrum. In simulations, the implosion performance was degraded by increasing the peak amplitude of the velocity perturbation spectrum. The 1-D degradation is incorporated as a degradation in the implosion velocity of the target, i.e., degradation in the initial condition

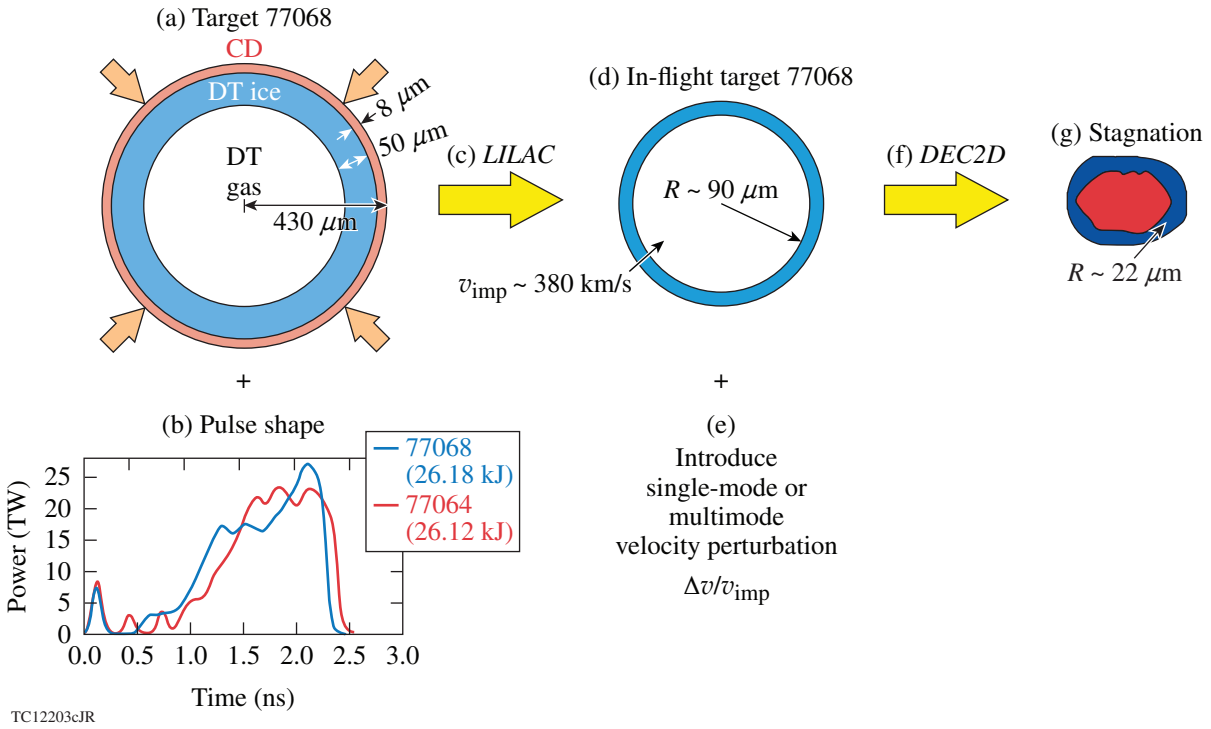

Figure 154.3
The procedure involved in the reconstruction technique. The (a) target and (b) pulse shape are used as initial conditions for the 1-D hydrodynamic code *LILAC*, which is used to (c) simulate the acceleration phase of implosions. The hydrodynamic profiles from the (d) in-flight target simulation are transferred to *DEC2D*; single- or multimode velocity perturbations are (e) introduced at the inner surface of the shell. (f) The deceleration phase of the implosion is simulated in 2-D, and (g) the stagnation parameters are extracted from these simulations.

of the deceleration-phase simulations; this has been denoted using "1-D v_{imp}." The scaling of the implosion observables with v_{imp} will be shown in the following sections. They are in reasonable agreement with Ref. 22, which instead uses a set of optimally performing *LILAC* simulations.

The single-picket pulse shape and target from OMEGA shot 77068 (used in this analysis) are shown in Fig. 154.3(b) (see blue curve). The analysis technique is very robust and can be applied to any implosion and any scale. The choice of shot 77068 was motivated by the fact that this was the best shot in terms of performance metric $\chi_{no\,\alpha}$ (Refs. 1 and 2) and other experimental observables such as yield and areal density. The target was driven with 26.18 kJ of laser energy to an implosion velocity of 380 km/s. The experimental observables, the 1-D simulation parameters, and the reconstructed observables for this shot are shown in Table 154.II. Notice that the experimental observables were reproduced using a combination of (1) the mid-modes component and (2) the low-mode component; a degradation of the simulated 1-D performance with either the low or mid modes alone would not produce the estimated results (this can be shown using the last two columns of Table 154.II). The velocity perturbation used for the reconstruction of shot 77068 is shown in Fig. 154.4; it consists of a combination of low-mode ($\ell = 2$) and mid-mode (a spectrum of mid modes) asymmetries. Figure 154.5 shows the shape of the hot spot and shell at the time of peak neutron production (i.e., bang time t_b); the final shape resembles a combination of a low-mode $\ell = 2$ and a dominant mid-mode $\ell = 10$. We emphasize that the exact mode numbers

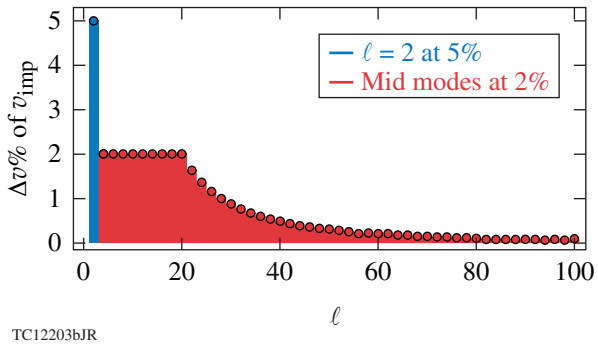

Figure 154.4
The initial velocity perturbation spectrum $\Delta v/v_{imp}\%$ (ℓ) that was used to synthetically reconstruct shot 77068 observables.

Table 154.II: Comparison of measurements with 1-D simulations (using *LILAC* and *DEC2D*) and 2-D simulations (using *DEC2D*).

Observables	Experiment shot 77068	1-D simulation	Reconstructed shot 77068	Mid modes component (1)	$\ell = 2$ component (2)	Mid modes $Y/Y_{1\text{-D}} \approx 0.3$	$\ell = 2$ $Y/Y_{1\text{-D}} \approx 0.3$
Yield	5.3×10^{13} (±5%)	1.7×10^{14}	5.3×10^{13}	7.9×10^{13}	9.8×10^{13}	5.3×10^{13}	5.3×10^{13}
P^* (Gbar)	56 (±7)	97	57	77	73	66	50
T_i (keV)	3.6 (±0.3)	3.82	3.70	3.78	3.71	3.64	3.42
R_{hs} (μm)	22 (±1)	22	22	20.9	23.4	21	25.3
t (ps)	66 (±6)	61	54	55	56	53	59
ρR (g/cm^2)	0.194 (±0.018)	0.211	0.194	0.222	0.193	0.211	0.180

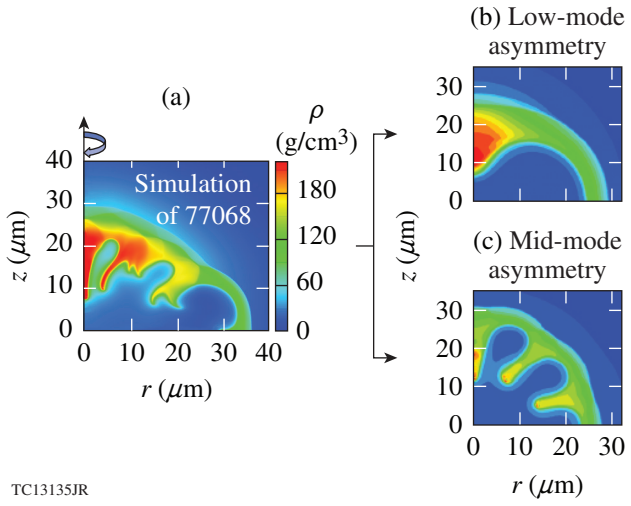

Figure 154.5
Plots illustrating a combination of low and mid modes that were used to reconstruct the core conditions of shot 77068. The density profiles at time of peak neutron production are shown for (a) reproduced shot 77068 with $Y/Y_{1\text{-D}} \approx 0.3$, (b) the low-mode $\ell = 2$ component at $Y/Y_{1\text{-D}} \approx 0.6$, and (c) an equivalent mid-mode $\ell = 10^*$ component at $Y/Y_{1\text{-D}} \approx 0.6$.

degrading the experimental performance cannot be inferred from this analysis technique, and other combinations of modes could also lead to the same reconstructed observables. However, the overall balance between the degradation by low modes and the degradation by mid modes on all of the observables must be preserved. To illustrate this, we also show trends from a different low mode: the $\ell = 1$ mode and the $\ell = 2$ asymmetry with a reversed phase. Although these modes are structurally different, the resulting trends are the same; for example, see trends in pressure and volume degradation in Figs. 154.6, 154.8, 154.12, 154.14, and 154.15. A discussion on the mode $\ell = 1$ asymmetry and an alternative reconstruction is shown in Appendix A of Ref. 23. Similarly, the mid modes (of the spectrum in Fig. 154.4) produces very similar degradation trends as the mode $\ell = 10^*$.

The following sections show the analysis of the 50-Gbar implosion results using this technique. The effect of low and mid modes on each of the implosion observables is discussed.

1. Inferred Hot-Spot Pressure

The hot-spot pressure is not directly measurable but it is inferred from other experimental observables using[24]

$$\frac{P_{\text{inf}}}{P_{\text{inf, l-D}}} = \sqrt{\left(\frac{Y}{Y_{\text{1-D}}}\right)\left(\frac{V}{V_{\text{1-D}}}\right)^{-1}\left[\frac{\left\langle \sigma v \right\rangle / T_i^2}{\left\langle \sigma v \right\rangle / T_i^2)_{\text{1-D}}}\right]^{-1}\left(\frac{\tau}{\tau_{\text{1-D}}}\right)^{-1}}, \quad (1)$$

where Y is the implosion yield obtained from experiments or simulations and is normalized with the 1-D yield ($Y_{1\text{-D}}$) from simulations. The $V/V_{1\text{-D}}$ is the normalized volume of the hot spot, calculated from the x-ray images of experiments or simulations. The fusion reactivity is a function of temperature only,[25] with $\sigma \approx 1$ to 2 for the temperature range of interest to ICF. The neutron burnwidth τ is the full width at half maximum of the neutron rate. The degradation trends for each of these observables will be shown in the following sections.

The degradation in pressure corresponding to a given degradation in yield is shown in Fig. 154.6. The degradation in inferred pressure is an outcome of the degradation in all of the measurable parameters shown in Eq. (1). For any yield degradation level, the low modes (in blue) result in a greater degradation of the hot-spot pressure as compared to mid modes (in red). The $\ell = 1$, $\ell = 2$, and $\ell = 2$ phase reversed produce nearly identical pressure degradation curves; also the $\ell = 10^*$ and mid modes produce similar curves. This is because for implosions with mid-mode asymmetries, the hot-spot volume is smaller as a result of cooling by penetration of the RTI spikes, but for low modes the volume is larger (see the next subsection). The

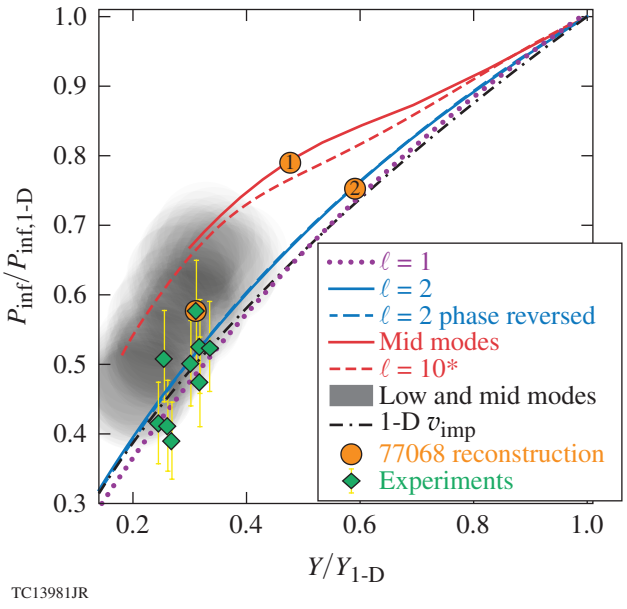

Figure 154.6
The degradation in inferred hot-spot pressure P_{inf}, normalized with 1-D pressure ($P_{inf,1\text{-}D}$), versus degradation in yield ($Y/Y_{1\text{-}D}$). This pressure is computed using Eq. (1) and the x-ray volume. The 50-Gbar shots in Table 154.I are shown in green. Reconstructed shot 77068 is shown in orange (overlapping the experimentally inferred pressure for shot 77068), with points (1) and (2) representing the degradation caused separately by the mid-mode and low-mode components. The gray-shaded region represents an ensemble of simulations using different amplitude combinations of $\ell = 2$ and mid modes; it is observed that these reproduce the experiments approximately.

gray-shaded region represents an ensemble of simulations using different amplitude combinations of $\ell = 2$ and mid modes, with the $\ell = 2$ amplitude varying between 4% and 7% of v_{imp} and the mid-mode amplitude varying between 2% and 4% of v_{imp}. The initial velocity perturbation spectrum of Fig. 154.4 could be used to reproduce the experimental pressure for shot 77068. The dashed–dotted black line in Fig. 154.6 shows the 1-D pressure scaling with implosion velocity; it follows $P_{inf} \sim v_{imp}^{3.72}$. The corresponding yield scaling with implosion velocity follows $Y \sim v_{imp}^{6.26}$. The implosion velocity degradation is a simplistic method to model the degradation in implosion convergence; it is useful for comparing trends. In experiments, degradation in implosion convergence can be caused by the following: very short scale nonuniformities arising from laser imprinting or reduced laser-to-capsule drive with respect to simulation, and preheating caused by superthermal electrons (which decrease the implosion convergence by increasing the implosion adiabat α).

Notice that in Fig. 154.6 the pressure degradation curve for the 1-D v_{imp} coincides with the low-mode curves ($\ell = 1$, $\ell = 2$, and $\ell = 2$ phase reversed), but is different from the mid-mode curves ($\ell = 10^*$ and mid modes). This can be explained based on Ref. 3. First, the hot spot is not isobaric for implosions with mid-mode asymmetries; second, the inferred pressure for mid modes is the average pressure of the x-ray–producing region of the hot spot. The x-ray–producing volume, however larger than the neutron-producing volume, is still smaller than the total hot-spot volume including the bubbles (i.e., $V_{\langle hs \rangle}$ of Ref. 3). As a result, the inferred pressure for implosions with mid-mode asymmetry using the x-ray volume is higher than the average hot-spot pressure. However, for the low-mode asymmetry or 1-D v_{imp} degradation curves (Fig. 154.6) the hot spot is approximately isobaric and the neutron and x-ray volumes are comparable to the total hot-spot volume ($V_{\langle hs \rangle}$, see Fig. 7 of Ref. 3); therefore, the inferred pressures are similar. If the neutron-producing volume is used instead of the x-ray volume, the inferred pressure for mid modes would be similar to the clean (1-D) value—irrespective of the yield, also shown in Fig. 7 of Ref. 3. In summary, the inferred pressure for implosions with mid-mode asymmetry is higher than that of low modes at the same yield-degradation level, as a result of a non-isobaric hot spot and a smaller hot-spot volume for the former.

2. Estimation of the Hot-Spot Size: Using Time-Gated Self-Emission Images

Time-resolved images of the core x-ray self-emission, as shown in Fig. 154.7, have been used to estimate the hot-spot volume.[12] Here R_{17} is the radius at 17% of peak intensity and $V_{x\ ray}/V_{x\ ray,1\text{-}D} = \left(R_{17}/R_{17,1\text{-}D}\right)^3$.

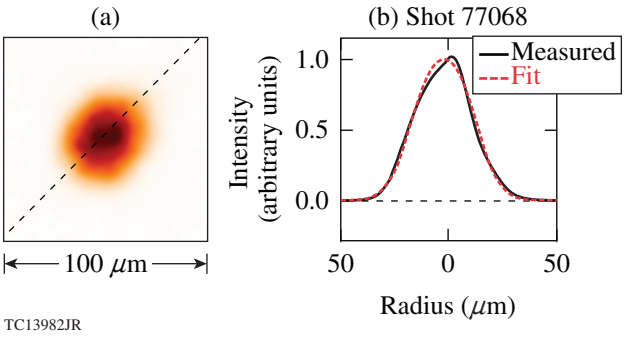

Figure 154.7
(a) An x-ray image of the hot spot at stagnation for shot 77068, obtained using a time-resolved Kirkpatrick–Baez (KB) framed camera with a 4- to-8 keV photon energy range and a 6-μm spatial resolution.[12] (b) The measured and fit x-ray profiles along the dashed line.

The effect of asymmetries on the hot-spot volume is shown in Fig. 154.8, where with increasing mode amplitude, the x-ray volume increases for low modes and decreases for mid modes. By cooling the plasma within the RTI bubbles, mid-mode asymmetries cause a reduction in the x-ray–emitting volume.

The gray-shaded region (representing the ensemble of simulations) shows that the volume estimated using a combination of low and mid modes is in agreement with the measured volume for the 50-Gbar shots, illustrating that the experiments can be reconstructed using such combinations of low and mid modes. The effect of an implosion velocity degradation on the x-ray volume has been shown using the dashed black line (1-D v_{imp}); it follows the scaling $V_{x\ ray} \sim v_{imp}^{-2.14}$. Notice that this curve coincides with the low-mode curves, but it is different from the mid-mode asymmetry curves for the same reasons as previously explained.

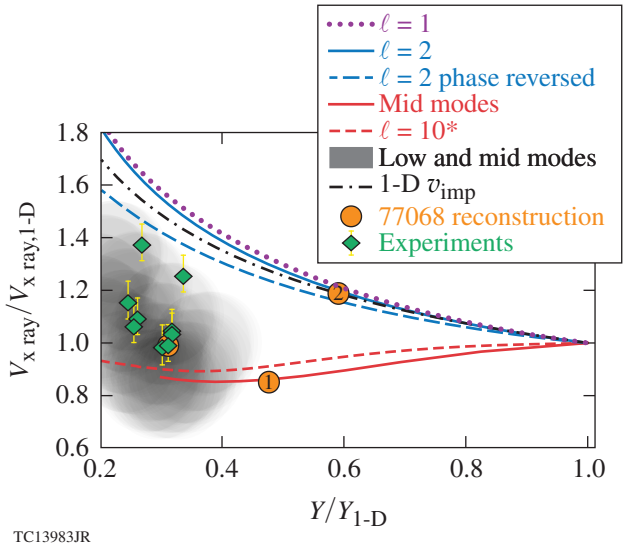

Figure 154.8
Plot showing the volume of the hot spot, obtained from time-resolved x-ray images and normalized with the 1-D volume $\left(V_{x\ ray}/V_{x\ ray,1\text{-}D}\right)$, versus the yield degradation $Y/Y_{1\text{-}D}$. The 50-Gbar shots in Table 154.I are shown in green. The reconstructed shot 77068 is shown in orange (overlapping the x-ray volume for shot 77068), with points (1) and (2) representing the degradation caused by the mid- and low-mode components, separately. The gray-shaded region represents an ensemble of simulations using different amplitude combination of $\ell = 2$ and mid modes; it is observed that these reproduce the experiments.

The disassembly phase of implosions is different for low- and mid-mode asymmetries. The physical mechanism involved has been discussed in Ref. 3. In this section we discuss signatures in time-resolved x-ray images that could aid the detection of mid modes. Time-resolved x-ray images (i.e., with 10-ps gate width) were produced from the simulations using the atomic physics code *Spect3D*.[26,27] These images were normalized with the maximum intensity for each image and fit with the following function:

$$f(x,y) = e^{-\left[(x/a)^2+(y/b)^2\right]^{\eta/2}}. \qquad (2)$$

The R_{17} was obtained from the fit using

$$R_{17} = \sqrt{a \times b}\left[\log(0.17)\right]^{1/\eta}.$$

The index η represents the index of the super-Gaussian fit, with $\eta = 2$ representing a Gaussian function. Figure 154.9 shows that during the disassembly (i.e., for $t > t_b$), the R_{17} decreases with time for mid modes, whereas it increases for low modes with respect to 1-D. A similar trend was also observed for other arbitrary definitions of the radius, i.e., radius at 37%, 50%, and 75% of peak intensity. Since detecting mid modes in experiments is challenging (because of the limited spatial resolution of the detectors), the above time-evolution trends in the x-ray images could motivate future experiments.

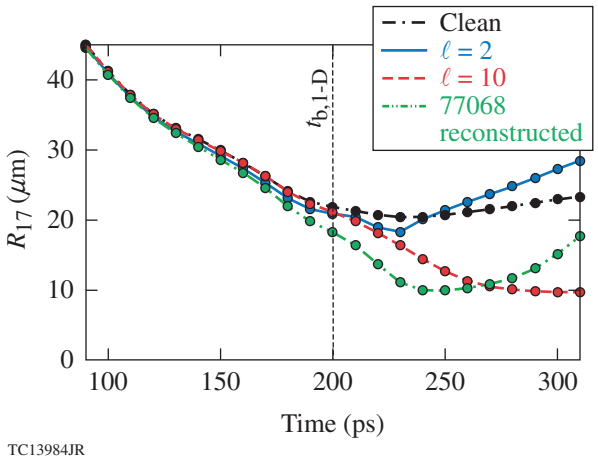

Figure 154.9
Plot showing the time evolution of the x-ray R_{17} obtained from simulations. This is shown for the symmetric case (black curve), low-mode $\ell = 2$ case with $Y/Y_{1\text{-}D} = 0.6$ (blue curve), mid-mode $\ell = 10$ case with $Y/Y_{1\text{-}D} = 0.6$ (red curve), and the reproduced case with $Y/Y_{1\text{-}D} \approx 0.3$ (green curve) for simulations of shot 77068.

3. Shape Analysis of Time-Integrated Self-Emission Images

In this section we discuss how asymmetries influence the time-integrated x-ray images. Since the photon statistics (i.e., determined by the number of incident photons) are insufficient for the 10- to-15-ps time-gated images (in the previous section), we do not use those images to infer the shape of the hot spot; instead we use the time-integrated images obtained using the gated monochromatic x-ray imaging (GMXI) module.[28] In Fig. 154.10 the first column shows the density profile and plasma-flow pattern at bang time. The corresponding synthetic self-emission images along with lineouts across a different axis are shown in the second and third columns, respectively. The cross sections were taken through the center

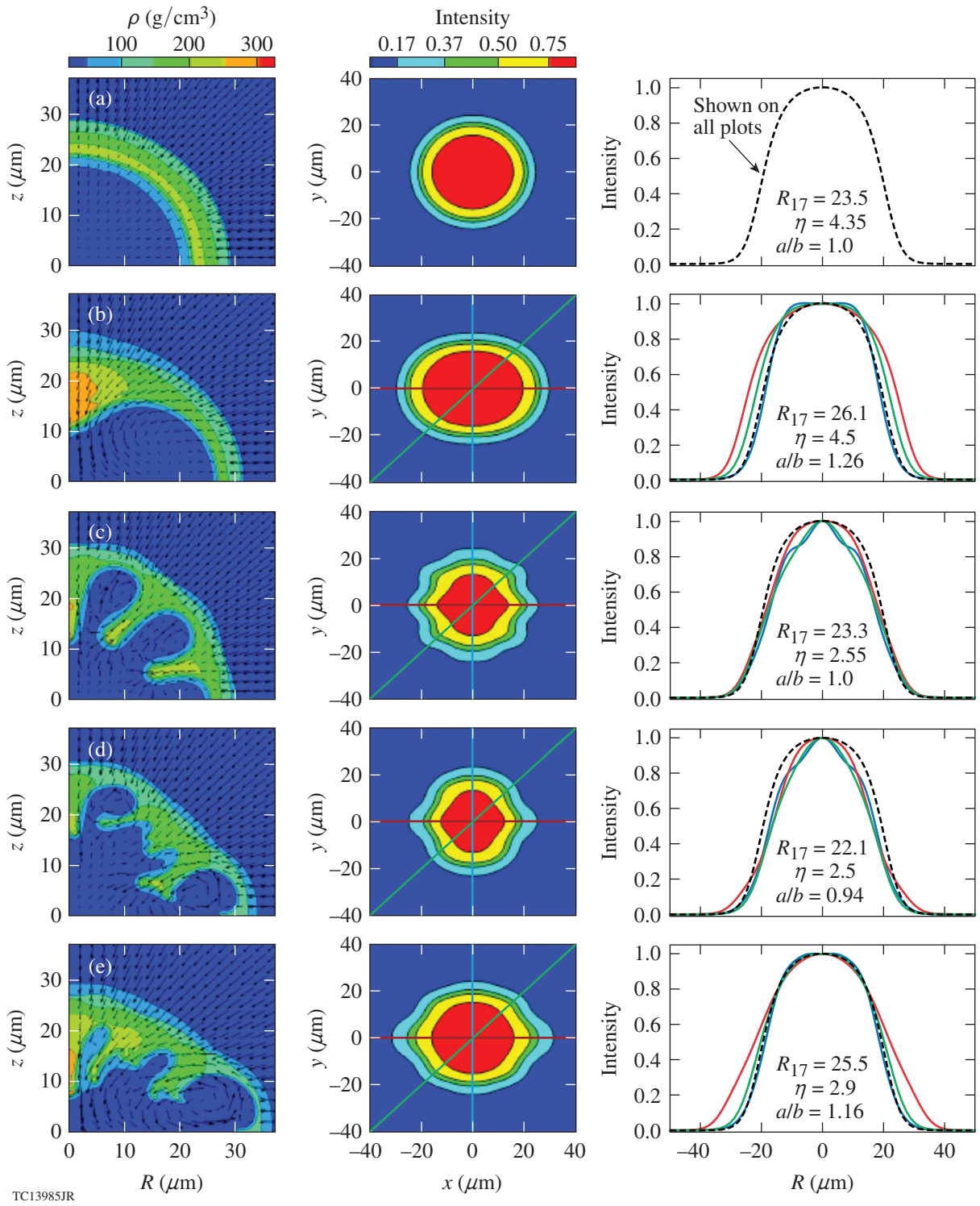

Figure 154.10
Contour plots of the density profile and plasma flow pattern at bang time (first column), time-integrated synthetic x-ray emission images (second column), and image lineouts (third column). The black dashed line represents the lineout of the symmetric image; it is shown on all plots in the third column for reference. The lineouts along the three different axes are labeled with different colors (red, blue, and green). The 2-D super-Gaussian fit parameters have been included. The images for (a) symmetric implosion, (b) $\ell = 2$ at $Y/Y_{1\text{-D}} = 0.6$, (c) $\ell = 10^{*}$ at $Y/Y_{1\text{-D}} = 0.6$, (d) mid modes (spectrum) with 2% ΔV at $Y/Y_{1\text{-D}} = 0.47$, and (e) reconstructed shot 77068 are shown.

of the image; they are marked on the contour plot with the same color as on the intensity plot. The x-ray images were reconstructed with the same filter, point spread function (PSF), and detector response as the experimental shot 77068; i.e., filtered with 6.5 mil of Be and 2 mil of Al, which transmit x rays in the 4- to 8-keV range, and a 7.5-μm PSF. The images were fit using the function shown in Eq. (2). The R_{17} of the time-integrated images, the ellipticity parameter (a/b), and the super-Gaussian exponent η were calculated from the fit. It was found that low modes cause an increase in the a/b and R_{17}, with the index η comparable or larger than the 1-D case. In comparison, mid modes cause a reduction in the index η because the mid modes exhibit several low-temperature bubbles surrounding the hot center, producing a more-gradual intensity variation with radius. The mid modes have a negligible effect on the calculated a/b and R_{17}.

Table 154.III shows the properties of the time-integrated x-ray images for the 50-Gbar shots. It is observed that for all of the shots, the time-integrated R_{17} is larger than the time-resolved images by 3 to 4 μm (see Table 154.I). This is in consistent agreement with our analysis showing that the time-integrated radius (R_{17}) is larger than the radius at bang time for low modes ($\ell = 2$) in simulations. The $\eta < \eta_{1\text{-D}}$ indicates the presence of mid modes and $a/b > 1$ indicates the presence of low modes in the implosions.

Table 154.III: The properties for the time-integrated GMXI[28] x-ray images from experiments.

Shot	R_{17} (mm) ±0.5 mm	η ±0.2	a/b ±0.01	Filter 6.5 mil Be+
78959	25.6	2.7	1.16	3 mil Al
78963	28.1	2.3	1.17	3 mil Al
78967	26.7	2.3	1.16	3 mil Al
78969	27.4	2.6	1.16	3 mil Al
78971	27.1	1.9	1.20	3 mil Al
77064	27.7	2.6	1.11	2 mil Al
77066	26.8	2.6	1.10	2 mil Al
77068	26.7	2.69	1.16	2 mil Al
77070	25.9	2.56	1.13	2 mil Al

Figure 154.11 shows the time-integrated image for shot 77068 and the reconstructed image. The agreement in shape and other parameters (R_{17}, a/b, and η) supports the presence of systematic mid modes along with low modes in the 50-Gbar implosions. In summary, low modes increase the ellipticity parameter (a/b) and radius (R_{17}) with respect to 1-D from the time-integrated x-ray images, and mid modes produce a lower super-Gaussian index η. A combination of low- and mid-mode asymmetries can be used to reproduce the experimental images.

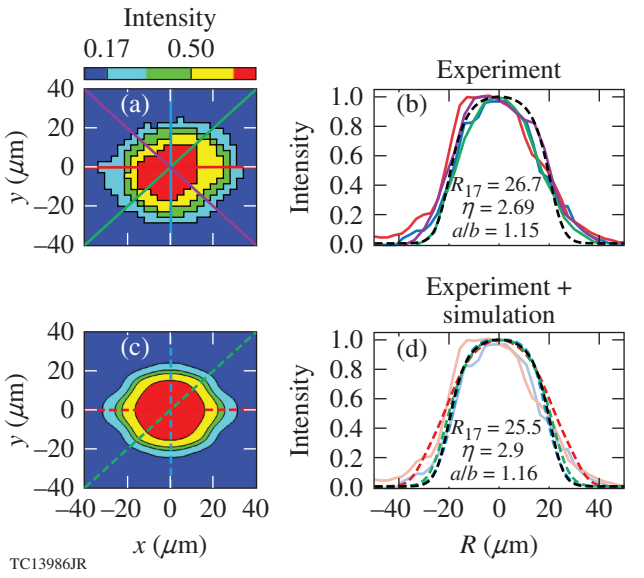

Figure 154.11
A comparison between time-integrated x-ray images for shot 77068 obtained from [(a) and (b)] experiments and [(c) and (d)] the reconstructed simulation. The lineouts along the different axes are labeled with different colors (red, blue, green, and purple), the lineouts for the experimental image are represented using solid curves [in (b) and (d)], and the simulations are represented using dashed curves [in (d)]. The lineout for the symmetric case is shown with black dashed curve [in (b) and (d)] for reference. The super-Gaussian fit parameters for both (b) experiment and (d) simulation are listed.

4. Neutron-Averaged Ion Temperature

Figure 154.12 shows the degradation in ion temperature $\left(T_i / T_{i,\,1\text{-D}}\right)$ with degradation in yield ($Y/Y_{1\text{-D}}$). It is observed that asymmetries cause a small degradation in $T_i / T_{i,\,1\text{-D}}$, within 10% to 15% of the 1-D value, for all yield degradation levels above $Y/Y_{1\text{-D}} > 0.2$. This is because the temperature of the region of the hot spot that produces fusion neutrons, i.e., the hot region, is only marginally affected by asymmetries (see Ref. 3). The results from simulations with a combination of low- and mid-mode asymmetries are in the gray-shaded area. The green diamonds, representing the 50-Gbar experiments, fall within the gray-shaded region. The temperature scaling with implosion velocity follows $T_i \sim v_{imp}^{0.91}$ in 1-D, which is estimated from the dashed black curve. It is observed that at the same yield degradation ($Y/Y_{1\text{-D}}$) level, the temperature is lower for the curve representing implosion velocity degradation (1-D v_{imp}) as compared to asymmetries.

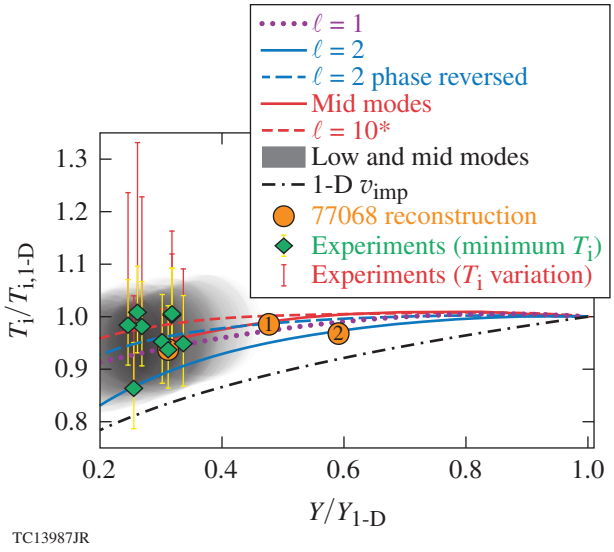

Figure 154.12
Plot showing degradation in neutron-averaged ion temperature $\left(T_i/T_{i,1\text{-}D}\right)$ versus the degradation in yield ($Y/Y_{1\text{-}D}$). The points in green represent the minimum ion temperature measured for the 50-Gbar shots; the red bar associated with each data point extends to the maximum ion temperature measurement. The reconstructed shot 77068 is shown in orange (overlapping with data); the points (1) and (2) represent degradation caused by the mid-mode and low-mode components separately. The gray-shaded region represents an ensemble of simulations using different amplitude combination of $\ell = 2$ and mid modes; it is observed that these reproduce the experiments.

The variation in ion-temperature measurements between detectors is shown by the red bars in Fig. 154.12; the length of the red bar represents the maximum variation $\Delta T_{max} = T_{i,max} - T_{i,min}$ between measurements along different lines of sight for the shot. It is known that flows[29–31] in the neutron-producing region of the hot spot, marked with arrows in Fig. 154.10 (first column), can affect the temperature measurements. This results in a higher apparent temperature, depending on the detector line of sight. The 50-Gbar implosions exhibit a considerable variation in ion-temperature measurements. The maximum variation in neutron-averaged ion temperature (ΔT_{max}) versus yield degradation level is also shown in Fig. 154.13. The experiments (represented by the green diamonds) exhibit shot-to-shot variation in ΔT_{max}, which is possibly caused by the differences in flow effects along different lines of sight. For the simulations, the apparent temperatures (i.e., including flow effects) were calculated using the Murphy[32] formulation [see Eq. (20) of Ref. 32]

$$T_{sp/bub}^{(app)}\,[\text{keV}] = T_i\,[\text{keV}] + \left(m_\alpha + m_n\right)\left\langle v_{sp/bub}^2\right\rangle[\text{keV}] \quad (3)$$

with

$$T_i = \frac{\iint T n_D n_T \langle\sigma v\rangle \, dV dt}{\iint n_D n_T \langle\sigma v\rangle \, dV dt}, \quad (4)$$

$$\left\langle v_{sp/bub}^2\right\rangle = \frac{\iint v_{sp/bub}^2 n_D n_T \langle\sigma v\rangle \, dV dt}{\iint n_D n_T \langle\sigma v\rangle \, dV dt} \quad (5)$$

for which we estimate (approximately) the neutron-averaged flow broadening along the spike or bubble axis using the above Eqs. (3)–(5). In the simulations (except the $\ell = 2$ phase-reversed case) the spike axis corresponds to the z axis (represented by subscript "sp") and the bubble axis is the r axis (represented by subscript "bub") (see Fig. 154.5; see Fig. 154.10 for the velocity flow field). Notice that the apparent temperature $T_{sp/bub}^{(app)} \geq T_i$ is the neutron average temperature. The maximum variation possible is estimated using the following

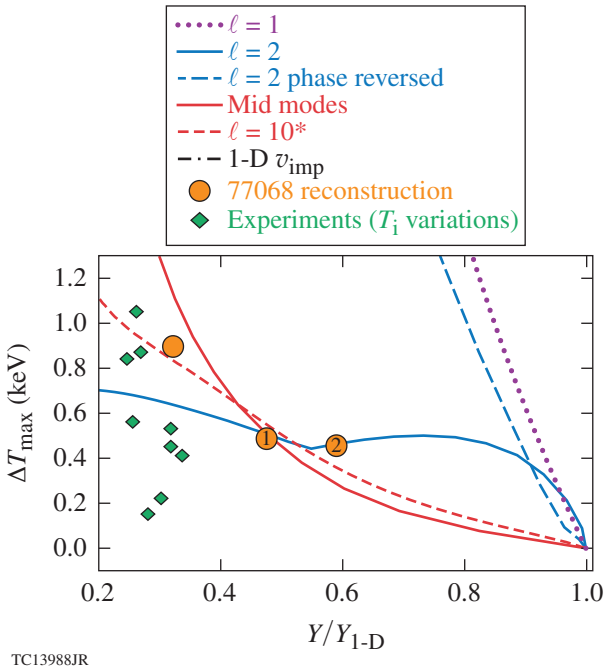

Figure 154.13
Plot showing the maximum variation in ion-temperature measurements (ΔT_{max}) versus degradation in yield ($Y/Y_{1\text{-}D}$). For the 50-Gbar experiments (green diamonds), the ΔT_{max} is given by $\Delta T_{max} = T_{i,max} - T_{i,min}$ across measurements along different lines of sight. The simulations show the maximum variation in ion temperature (ΔT_{max}) estimated using Eq. (6). The reconstructed shot 77068 is shown in orange, with points (1) and (2) representing the degradation caused by the mid- and low-mode components, separately.

$$\Delta T_{max} = \max\left[T_{sp}^{(app)}, T_{bub}^{(app)}\right] - T_i, \quad (6)$$

where $T_{sp}^{(app)}$ [or $T_{bub}^{(app)}$] is the apparent temperature measured by a detector sitting on the spike axis [or bubble axis] and T_i is the neutron-averaged ion temperature calculated without including the flow effects (as expected, the variation in ion temperature is negligible for symmetric implosions). We find that the ΔT_{max} from experiments and the calculated ΔT_{max} are comparable for implosions with $\ell = 2$ and mid modes. The $\ell = 1$ mode and the phase-reversed low mode ($\ell = 2$ phase reversed) produce higher variations in apparent temperature than others in the simulations because these implosions are influenced by significant bulk flow motion within the relatively large neutron-producing volume.

Our technique, which uses a combination of low and mid modes, can be used to consistently reproduce the neutron-averaged temperature measurements and estimate the variation in temperature for the 50-Gbar experiments.

5. Implosion Areal Density

The effect of asymmetries on the areal density (ρR) is discussed in this section. The ρR's estimated from the down-scattered ratio (DSR) of the neutron spectrum obtained from experiments and simulations are shown in Fig. 154.14. It is observed that the measured ρR's are comparable to the corresponding 1-D estimated values (from *LILAC*) although the yields are heavily degraded ($Y/Y_{1\text{-D}} \sim 0.3$) in the experiments. In Fig. 154.14, the ρR scaling with symmetric yield (produced by decreasing the implosion velocity) is shown by the dashed black curve (1-D v_{imp}); it follows $\rho R \sim v_{imp}^{1.42}$. In the simulations the ρR's are calculated using the Monte Carlo neutron-tracking post-processor code *IRIS3D*.[33] Notice that the ρR for implosions with asymmetries is always higher than the 1-D v_{imp} curve. The ρR is a parameter dependent on the implosion convergence; for symmetric implosions the yield and ρR decrease with decreasing convergence according to the 1-D v_{imp} curve of Fig. 154.14. Instead, for distorted implosions, the convergence of the spikes can be high, producing a relatively higher ρR, but this does not increase the yield (see Ref. 3). The ρR for implosions with mid-mode asymmetry (represented by the $\ell = 10^*$ and mid-mode curves) is comparable to the estimated $\rho R_{1\text{-D}}$. This is because for mid modes, multiple RTI spikes approach the implosion center, producing a compressed plasma with a higher ρR. For the low-mode cases ($\ell = 1$, $\ell = 2$, and $\ell = 2$ phase reversed), this effect is relatively small; nevertheless, the ρR's at any given $Y/Y_{1\text{-D}}$ are higher than the 1-D ρR versus yield scaling (represented by the 1-D v_{imp}).

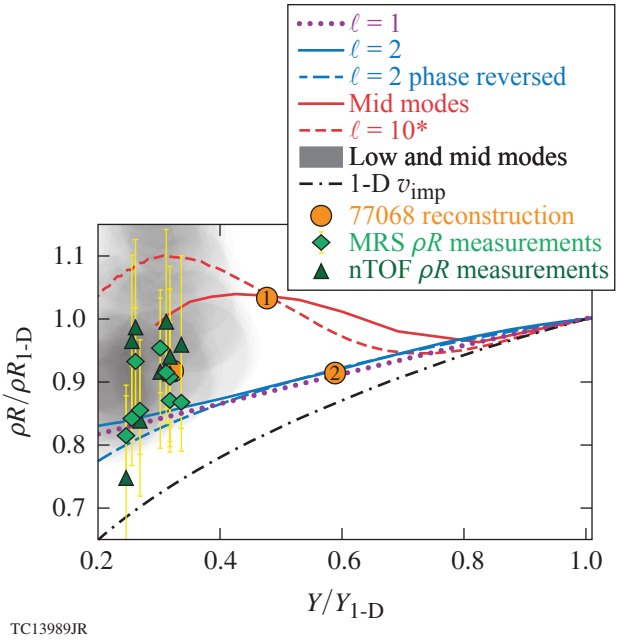

Figure 154.14
Plot showing the degradation in areal density (i.e., ρR estimated from DSR) versus degradation in yield. The ρR and yield are normalized with the 1-D estimated values. The neutron time-of-flight (nTOF, triangles) and magnetic recoil spectrometer (MRS, diamonds) ρR measurements for the 50-Gbar shots are shown in green. The reconstructed shot 77068 is shown in orange (overlapping with data), with points (1) and (2) representing degradation caused by the mid-mode and low-mode components, separately. The gray-shaded region represents an ensemble of simulations using different amplitude combinations of $\ell = 2$ and mid modes; it is observed that these reproduce the experiments.

A combination of low and mid modes (shown by the gray-shaded region) could be used to reconstruct the ρR for the 50-Gbar shots (shown as green triangles and diamonds). The measurements along with consideration of the asymmetry trends suggest that a fraction of the measured ρR is provided by the cold spikes and ablated mass accumulated in the bubbles surrounding the burn volume; therefore, they do not contribute to fusion-yield production but augment the areal density.

6. Burnwidth and Bang Time

Figure 154.15(a) shows a plot of burnwidth degradation ($\tau/\tau_{1\text{-D}}$) with yield degradation ($Y/Y_{1\text{-D}}$). It is observed that the burnwidths from NTD measurements are longer than the 1-D values (from *LILAC*), i.e., $\tau/\tau_{1\text{-D}} > 1$; however, the estimated error in the NTD burnwidths is ~±7 ps. The scaling of burnwidth with implosion velocity is represented using the 1-D v_{imp} curve; it follows $\tau \sim v_{imp}^{-1.2}$.

In simulations with asymmetries, the burnwidth shows a modest reduction with degradation in yield. However, for very large low-mode asymmetries (i.e., $Y/Y_{1\text{-D}} < 0.4$), the burnwidth

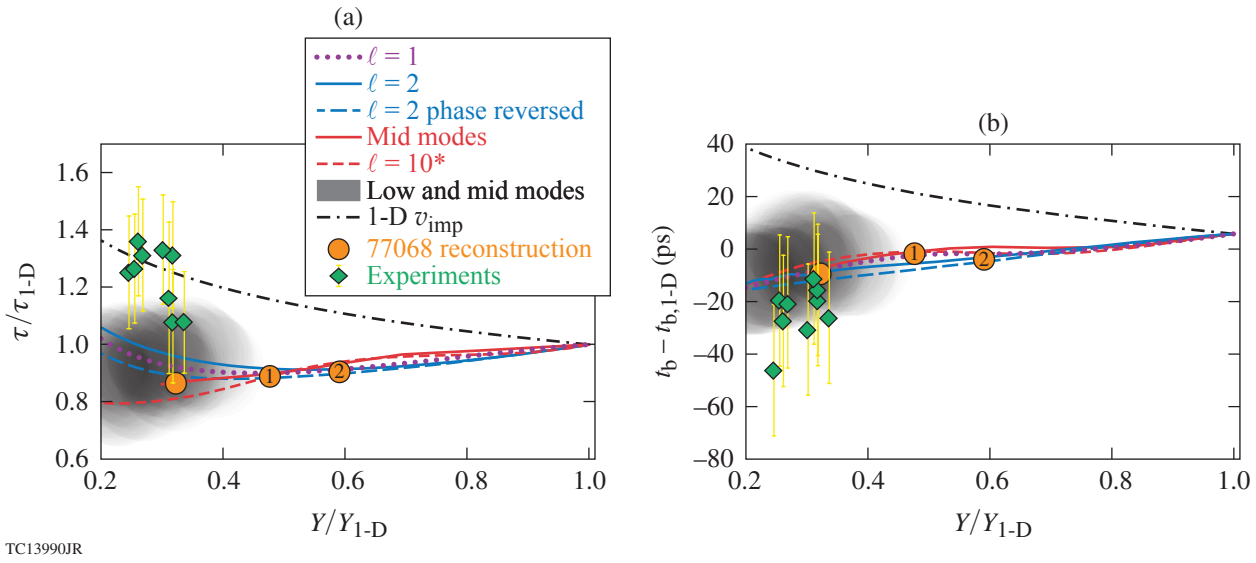

Figure 154.15
Plots showing (a) burnwidth ($\tau/\tau_{1\text{-D}}$) and (b) shift in bang time with respect to the 1-D simulations (i.e., $t_b - t_{b,1\text{-D}}$) versus degradation in yield ($Y/Y_{1\text{-D}}$). The green diamonds represent the experimental results from the 50-Gbar implosions (Table 154.I). The reconstructed shot 77068 is shown in orange; points (1) and (2) represent degradation caused by the mid-mode and low-mode components, separately. The gray-shaded region represents an ensemble of simulations using different amplitude combinations of $\ell = 2$ and mid modes.

increases with decreasing yield; this phenomenon has been described in Ref. 3. A combination of low and mid modes (shown in the gray-shaded region) produce burnwidths that are comparable to the 1-D estimated burnwidth (from *LILAC*) to within 30%, but, on average, they are shorter than the burnwidths for the 50-Gbar experiments.

Figure 154.15(b) shows a shift in bang time compared to the 1-D estimated values ($t_b - t_{b,1\text{-D}}$) with degradation in yield ($Y/Y_{1\text{-D}}$). The bang time from experiments (measured using the NTD) are shifted earlier in time; however, the estimated error in the NTD bang times are considerable ($\approx \pm 25$ ps). Notice that unlike burnwidths, this is in agreement with the asymmetry trends, which also shift the bang time forward, but it is opposite to what an implosion velocity (i.e., 1-D) degradation would do, as shown by the 1-D v_{imp} curve for which the bang time occurs later, i.e., $(t_b - t_{b,1\text{-D}}) > 0$.

We propose two possible explanations for the discrepancy between burnwidth and bang time. One possibility is the inaccuracy of the measurements. The NTD measurements for burnwidth and bang time have large error bars and probably are influenced by systematic effects that are not being considered here. It is possible that the actual burnwidths are 10 to 15 ps shorter and the actual bang times are 10 to 15 ps later than what are measured. The 10 to 15 ps in both burnwidth and bang time are within the measurement error. This would mean that both are consistent with the trends arising from asymmetries.

The second possible explanation is that in addition to a low mode (like $\ell = 1$ or $\ell = 2$) and a mid mode (like $\ell = 10$), there is a 1-D degradation in implosion convergence. This would mean that there is a systematic difference in the laser drive that is not accounted for by the laser–plasma coupling models (or equation-of-state model) in the *LILAC* simulations. Therefore the burnwidths are indeed longer, as measured by the NTD and predicted by the 1-D v_{imp} scaling curves. However, the bang time, which depends on the history of the acceleration phase, is not correctly captured by the simplistic deceleration-phase scaling (represented by the 1-D v_{imp} curves). In experiments, a degradation in implosion convergence can be caused by the following: very short scale nonuniformities arising from laser imprinting or reduced laser-to-capsule drive with respect to simulation, and preheating caused by super-thermal electrons (which decrease the implosion convergence by increasing the implosion adiabat α).

Conclusions and Future Application

This article discussed a technique to investigate the implosion performance degradation mechanisms based on trends in the experimental observables. This technique was applied to an ensemble of DT cryogenic implosions on OMEGA that

achieved hot-spot pressures of ~50 Gbar (Ref. 1). It was shown that a combination of low- and mid-mode asymmetries could be used to reconstruct the implosion core.[2] In addition to the presence of low modes, which cause a degradation of the stagnation pressure, it was shown that mid-mode asymmetries have a significant impact on the implosion performance. While it is challenging to image mid-mode asymmetries in implosions, this technique can be used to infer the effect of mid modes on the observables. It was shown that mid modes decrease the hot-spot size (i.e., time-resolved x-ray R_{17}) and lead to center-peaked, time-integrated x-ray images (i.e., a smaller super-Gaussian exponent η compared to a symmetric implosion). This occurs because the region of mid-mode bubbles surrounding the hot center introduces a gradual variation in the x-ray intensity. A consistent explanation for the ion-temperature, areal-density, volume, and pressure measurements for the 50-Gbar shots was described. The possible reasons behind the modest discrepancies between burnwidth and bang time were discussed based on the measurements and the predicted degradation trends.

Determining the exact mode numbers that degrade the experiments was not the goal of this article; other combinations of modes could also produce the observables simultaneously. The overall balance between the degradation by low modes and mid modes must be preserved. It was also shown that the trends in the implosion observables arising from an $\ell = 1$ asymmetry[34–36] are similar to the other low modes like the $\ell = 2$ or $\ell = 2$ with a reversed phase; only the ion-temperature variation introduced by the $\ell = 1$ mode or $\ell = 2$ with a reversed phase is higher than the $\ell = 2$ (or all other higher modes) and the experiments. In principle, it is challenging to distinguish between these modes given the quality of the experimental images.

This article complements the more detailed analysis of asymmetries provided in Ref. 3 with analysis of experiments. It was shown in Ref. 3 that the neutron-averaged observables can differ from the hot-spot volume-averaged quantities; the differences, although small for low modes, are more pronounced for mid-mode asymmetries. In other words, the energy distribution at stagnation is similar for both asymmetry types; however, the fusion reaction distribution is different. Also described is an analysis technique that ventures a consistent correlation between all the experimental observables of the implosion core, based on studies of asymmetries and 1-D degradation. It must be emphasized that this multi-objective prescription for analyzing cryogenic implosions simultaneously takes into account trends in all of the experimental observables, therefore providing leads to investigating systematic errors in measurements.

The analysis of several repeats of the cryogenic implosion experiments suggests a systematic degradation mechanism affecting the implosions. A combination of low and mid modes was used to reconstruct all the experimental observables pertaining to the core. It was shown that the experimental observables cannot be explained using either low- or mid-mode asymmetries separately; therefore, a combination was necessary for the reconstruction.

Quantitative measurements and mitigation of asymmetries in direct-drive implosions constitute a major component of the ongoing and future research at the Omega Laser Facility. To mention a few: A monochromatic backlighter using the short pulse from OMEGA EP has been developed to radiograph the cryogenic implosions on OMEGA.[37] Systematic low-mode asymmetries were observed using narrowband self-emission x-ray images from a titanium tracer layer placed at the fuel–shell interface.[38] Laser phase-plate designs are being investigated to improve laser coupling and drive symmetry.[39] Multiple self-emission x-ray images are being used to measure asymmetry modes up to the end of the laser drive, followed by adjustments in the laser beam energy balance to correct the asymmetry modes.[40] To motivate this effort, we provide an estimate of the implosion performance with improved implosion symmetry, i.e., by correcting the systematic and repeatably occurring asymmetries. It is estimated that mitigation of low- and mid-mode asymmetries would both result in an increase in the fusion yield, however, through an increase in the hot-spot pressure (from 56 Gbar to 80 Gbar) for low modes and an increase in the burn volume for mid-modes.

Figure 154.16 shows that an improvement in implosion core symmetry by correcting either the systematic mid or low modes, included in the reconstruction of shot 77068 (and other 50-Gbar shots[1]), can produce a burning plasma (i.e., $Q_\alpha \geq 1$, see Ref. 41) when extrapolated to a NIF-scale implosion core; i.e., an equivalent 1.9-MJ implosion with symmetric direct illumination (see Ref. 2). Note that the pressure values shown in Fig. 154.16 are relevant for the targets discussed in this article and serve only as an approximate gauge; in fact, implosion performance must be estimated using a Lawson-type metric like the $\chi_{\mathrm{no}\,\alpha}$. For extrapolated shot 77068, it is estimated that multidimensional effects produce a small uncertainty in the performance metric and the yield amplification factor. It was repeated in Ref. 16 that the $\chi_{\mathrm{no}\,\alpha} = 0.61$ produces a 2× amplification in yield in the simulation, in agreement with the 1-D alpha-heating model[41,42] and the fit formula: yield amplification $Y_{\mathrm{amp}} \approx \left(1 - \chi_{\mathrm{no}\,\alpha}/0.96\right)^{-0.75}$. In addition, it must be

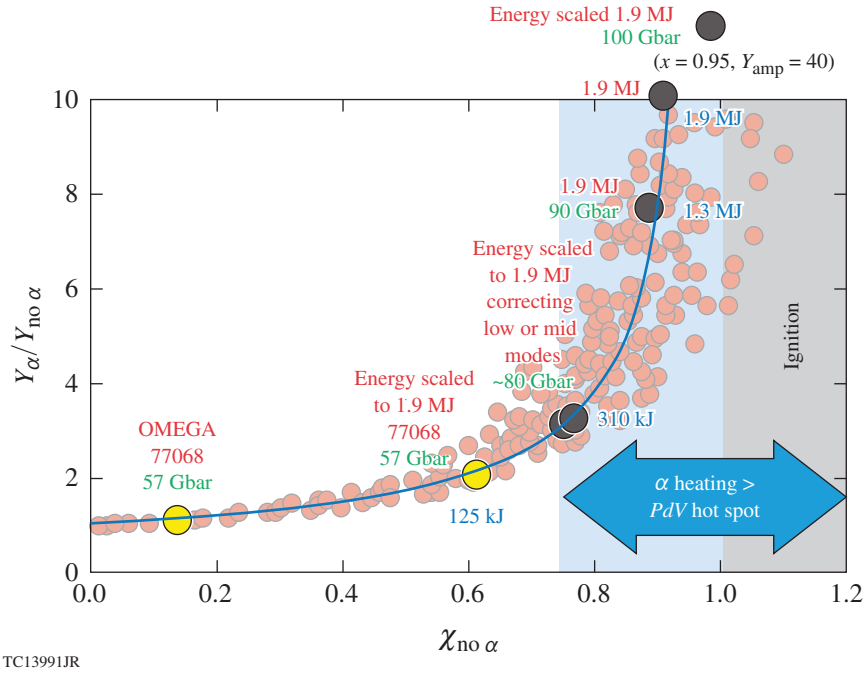

Figure 154.16

Plot of yield amplification versus $\chi_{no\,\alpha}$ (Ref. 41), where $\chi_{no\,\alpha}$ is estimated using Eq. (3) of Ref. 2; 1-D and 2-D simulation results (red circles) and $Y_\alpha / Y_{no\,\alpha} = \left(1-\chi_{no\,\alpha}/0.96\right)^{-0.75}$ (blue curve) are shown. The Lawson ignition condition $\chi_{no\,\alpha} \geq 1$ and the burning plasma regime $Q_\alpha \geq 1$ are shown by the gray- and blue-shaded regions, respectively. OMEGA shot 77068 (with 26 kJ of laser energy) and its equivalent implosion extrapolated to a 1.9-MJ driver[2] are shown (yellow circles); they exhibit inferred core pressures of 57 Gbar. Correcting either the low- or mid-mode component of this implosion can produce ≈80-Gbar pressure (see Table 154.II), with its performance approaching the burning plasma regime (simulation results are shown by black circles). Improving the asymmetry sources by 0.1× produces 90-Gbar pressure. The 1-D design has a hot-spot pressure of ≈100 Gbar with $\chi_{no\,\alpha} = 0.95$ and a yield amplification of $Y_{amp} = 40$. The fusion energy output corresponding to each of the extrapolated simulations is shown in blue. Shot 77068 when extrapolated to 1.9 MJ is estimated to produce 125 kJ of fusion energy—much higher (≈5×) than indirect-drive implosions at the same $\chi_{no\,\alpha}$. Improving the asymmetry sources by 0.01× is estimated to produce 1.9 MJ of fusion energy (the same as the laser driver). The relatively higher fusion energy output accentuates the advantage of the direct-drive approach over indirect drive with the same laser energy.

noted that in Fig. 154.16 the $\chi_{no\,\alpha}$ for other representative points (black circles) are increasingly accurate; this is because they are obtained by improving the implosion symmetry, as can be observed from the proximity of the simulation points (black circles) to the 1-D fit (blue curve).

In the future this analysis technique will be applied to different 1-D implosion designs (i.e., with different implosion adiabat, obtained from optimization of pulse shape and target dimensions), which would enhance the understanding and possibly lead to identification of the degradation sources for OMEGA direct-drive implosions.

ACKNOWLEDGMENT

This research has been supported by the U.S. Department of Energy under Cooperative Agreements DE-FC02-04ER54789 (Office of Fusion Energy Sciences) and DE-NA0001944 (National Nuclear Security Administration), the NYSERDA, and by the Lawrence Livermore National Laboratory under subcontract B614207.

REFERENCES

1. S. P. Regan, V. N. Goncharov, I. V. Igumenshchev, T. C. Sangster, R. Betti, A. Bose, T. R. Boehly, M. J. Bonino, E. M. Campbell, D. Cao, T. J. B. Collins, R. S. Craxton, A. K. Davis, J. A. Delettrez, D. H. Edgell, R. Epstein, C. J. Forrest, J. A. Frenje, D. H. Froula, M. Gatu Johnson, V. Yu. Glebov, D. R. Harding, M. Hohenberger, S. X. Hu, D. Jacobs-Perkins, R. T. Janezic, M. Karasik, R. L. Keck, J. H. Kelly, T. J. Kessler, J. P. Knauer, T. Z. Kosc, S. J. Loucks, J. A. Marozas, F. J. Marshall, R. L. McCrory, P. W. McKenty, D. D. Meyerhofer, D. T. Michel, J. F. Myatt, S. P. Obenschain, R. D. Petrasso, R. B. Radha, B. Rice, M. Rosenberg, A. J. Schmitt, M. J. Schmitt, W. Seka, W. T. Shmayda, M. J. Shoup III, A. Shvydky, S. Skupsky, A. A. Solodov, C. Stoeckl, W. Theobald, J. Ulreich, M. D. Wittman, K. M. Woo, B. Yaakobi, and J. D. Zuegel, Phys. Rev. Lett. **117**, 025001 (2016); **117**, 059903(E) (2016).

2. A. Bose, K. M. Woo, R. Betti, E. M. Campbell, D. Mangino, A. R. Christopherson, R. L. McCrory, R. Nora, S. P. Regan, V. N. Goncharov, T. C. Sangster, C. J. Forrest, J. Frenje, M. Gatu Johnson, V. Yu. Glebov, J. P. Knauer, F. J. Marshall, C. Stoeckl, and W. Theobald, Phys. Rev. E **94**, 011201(R) (2016).

3. A. Bose, R. Betti, D. Shvarts, and K. M. Woo, Phys. Plasmas **24**, 102704 (2017).

4. J. Delettrez, R. Epstein, M. C. Richardson, P. A. Jaanimagi, and B. L. Henke, Phys. Rev. A **36**, 3926 (1987).

5. I. V. Igumenshchev, W. Seka, D. H. Edgell, D. T. Michel, D. H. Froula, V. N. Goncharov, R. S. Craxton, L. Divol, R. Epstein, R. Follett, J. H. Kelly, T. Z. Kosc, A. V. Maximov, R. L. McCrory, D. D. Meyerhofer, P. Michel, J. F. Myatt, T. C. Sangster, A. Shvydky, S. Skupsky, and C. Stoeckl, Phys. Plasmas **19**, 056314 (2012).

6. V. N. Goncharov, T. C. Sangster, P. B. Radha, R. Betti, T. R. Boehly, T. J. B. Collins, R. S. Craxton, J. A. Delettrez, R. Epstein, V. Yu. Glebov, S. X. Hu, I. V. Igumenshchev, J. P. Knauer, S. J. Loucks, J. A. Marozas, F. J. Marshall, R. L. McCrory, P. W. McKenty, D. D. Meyerhofer, S. P. Regan, W. Seka, S. Skupsky, V. A. Smalyuk, J. M. Soures, C. Stoeckl, D. Shvarts, J. A. Frenje, R. D. Petrasso, C. K. Li, F. Séguin, W. Manheimer, and D. G. Colombant, Phys. Plasmas **15**, 056310 (2008).

7. O. A. Hurricane *et al*., Nature **506**, 343 (2014).

8. T. Döppner, D. A. Callahan, O. A. Hurricane, D. E. Hinkel, T. Ma, H. S. Park, L. F. Berzak Hopkins, D. T. Casey, P. Celliers, E. L. Dewald, T. R. Dittrich, S. W. Haan, A. L. Kritcher, A. MacPhee, S. Le Pape, A. Pak, P. K. Patel, P. T. Springer, J. D. Salmonson, R. Tommasini, L. R. Benedetti, E. Bond, D. K. Bradley, J. Caggiano, J. Church, S. Dixit, D. Edgell, M. J. Edwards, D. N. Fittinghoff, J. Frenje, M. Gatu Johnson, G. Grim, R. Hatarik, M. Havre, H. Herrmann, N. Izumi, S. F. Khan, J. L. Kline, J. Knauer, G. A. Kyrala, O. L. Landen, F. E. Merrill, J. Moody, A. S. Moore, A. Nikroo, J. E. Ralph, B. A. Remington, H. F. Robey, D. Sayre, M. Schneider, H. Streckert, R. Town, D. Turnbull, P. L. Volegov, A. Wan, K. Widmann, C. H. Wilde, and C. Yeamans, Phys. Rev. Lett. **115**, 055001 (2015).

9. O. A. Hurricane, D. A. Callahan, D. T. Casey, E. L. Dewald, T. R. Dittrich, T. Döppner, M. A. Barrios Garcia, D. E. Hinkel, L. F. Berzak Hopkins, P. Kervin, J. L. Kline, S. Le Pape, T. Ma, A. G. MacPhee, J. L. Milovich, J. Moody, A. E. Pak, P. K. Patel, H.-S. Park, B. A. Remington, H. F. Robey, J. D. Salmonson, P. T. Springer, R. Tommasini, L. R. Benedetti, J. A. Caggiano, P. Celliers, C. Cerjan, R. Dylla-Spears, D. Edgell, M. J. Edwards, D. Fittinghoff, G. P. Grim, N. Guler, N. Izumi, J. A. Frenje, M. Gatu Johnson, S. Haan, R. Hatarik, H. Herrmann, S. Khan, J. Knauer, B. J. Kozioziemski, A. L. Kritcher, G. Kyrala, S. A. Maclaren, F. E. Merrill, P. Michel, J. Ralph, J. S. Ross, J. R. Rygg, M. B. Schneider, B. K. Spears, K. Widmann, and C. B. Yeamans, Phys. Plasmas **21**, 056314 (2014).

10. A. Bose, K. M. Woo, R. Nora, and R. Betti, Phys. Plasmas **22**, 072702 (2015).

11. R. Nora, R. Betti, K. S. Anderson, A. Shvydky, A. Bose, K. M. Woo, A. R. Christopherson, J. A. Marozas, T. J. B. Collins, P. B. Radha, S. X. Hu, R. Epstein, F. J. Marshall, R. L. McCrory, T. C. Sangster, and D. D. Meyerhofer, Phys. Plasmas **21**, 056316 (2014).

12. F. J. Marshall, R. E. Bahr, V. N. Goncharov, V. Yu. Glebov, B. Peng, S. P. Regan, T. C. Sangster, and C. Stoeckl, Rev. Sci. Instrum. **88**, 093702 (2017).

13. G. J. Schmid, R. L. Griffith, N. Izumi, J. A. Koch, R. A. Lerche, M. J. Moran, T. W. Phillips, R. E. Turner, V. Yu. Glebov, T. C. Sangster, and C. Stoeckl, Rev. Sci. Instrum. **74**, 1828 (2003).

14. V. Yu. Glebov, D. D. Meyerhofer, C. Stoeckl, and J. D. Zuegel, Rev. Sci. Instrum. **72**, 824 (2001).

15. V. Yu. Glebov, C. J. Forrest, K. L. Marshall, M. Romanofsky, T. C. Sangster, M. J. Shoup III, and C. Stoeckl, Rev. Sci. Instrum. **85**, 11E102 (2014).

16. J. A. Frenje, D. T. Casey, C. K. Li, J. R. Rygg, F. H. Séguin, R. D. Petrasso, V. Yu. Glebov, D. D. Meyerhofer, T. C. Sangster, S. Hatchett, S. Haan, C. Cerjan, O. Landen, M. Moran, P. Song, D. C. Wilson, and R. J. Leeper, Rev. Sci. Instrum. **79**, 10E502 (2008).

17. C. Stoeckl, R. Boni, F. Ehrne, C. J. Forrest, V. Yu. Glebov, J. Katz, D. J. Lonobile, J. Magoon, S. P. Regan, M. J. Shoup III, A. Sorce, C. Sorce, T. C. Sangster, and D. Weiner, Rev. Sci. Instrum. **87**, 053501 (2016).

18. S. X. Hu, P. B. Radha, J. A. Marozas, R. Betti, T. J. B. Collins, R. S. Craxton, J. A. Delettrez, D. H. Edgell, R. Epstein, V. N. Goncharov, I. V. Igumenshchev, F. J. Marshall, R. L. McCrory, D. D. Meyerhofer, S. P. Regan, T. C. Sangster, S. Skupsky, V. A. Smalyuk, Y. Elbaz, and D. Shvarts, Phys. Plasmas **16**, 112706 (2009).

19. V. N. Goncharov, T. C. Sangster, R. Betti, T. R. Boehly, M. J. Bonino, T. J. B. Collins, R. S. Craxton, J. A. Delettrez, D. H. Edgell, R. Epstein, R. K. Follett, C. J. Forrest, D. H. Froula, V. Yu. Glebov, D. R. Harding, R. J. Henchen, S. X. Hu, I. V. Igumenshchev, R. Janezic, J. H. Kelly, T. J. Kessler, T. Z. Kosc, S. J. Loucks, J. A. Marozas, F. J. Marshall, A. V. Maximov, R. L. McCrory, P. W. McKenty, D. D. Meyerhofer, D. T. Michel, J. F. Myatt, R. Nora, P. B. Radha, S. P. Regan, W. Seka, W. T. Shmayda, R. W. Short, A. Shvydky, S. Skupsky, C. Stoeckl, B. Yaakobi, J. A. Frenje, M. Gatu-Johnson, R. D. Petrasso, and D. T. Casey, Phys. Plasmas **21**, 056315 (2014).

20. I. V. Igumenshchev, D. T. Michel, R. C. Shah, E. M. Campbell, R. Epstein, C. J. Forrest, V. Yu. Glebov, V. N. Goncharov, J. P. Knauer, F. J. Marshall, R. L. McCrory, S. P. Regan, T. C. Sangster, C. Stoeckl, A. J. Schmitt, and S. Obenschain, Phys. Plasmas **24**, 056307 (2017).

21. D. H. Edgell, R. K. Follett, I. V. Igumenshchev, J. F. Myatt, J. G. Shaw, and D. H. Froula, Phys. Plasmas **24**, 062706 (2017); *LLE Review Quarterly Report* **150**, 61, Laboratory for Laser Energetics, University of Rochester, Rochester, NY, LLE Document No. DOE/NA/1944-1331 (2017). Copies may be obtained from the National Technical Information Service, Springfield, VA 22161.

22. C. D. Zhou and R. Betti, Phys. Plasmas **14**, 072703 (2007).

23. A. Bose, R. Betti, D. Mangino, D. Patel, K. M. Woo, A. R. Christopherson, V. Gopalaswamy, S. P. Regan, V. N. Goncharov, C. J. Forrest, J. A. Frenje, M. Gatu Johnson, V. Yu. Glebov, J. P. Knauer, F. J. Marshall, R. Shah, C. Stoeckl, W. Theobald, T. C. Sangster, and E. M. Campbell, "Analysis of Trends in Implosion Observables for Direct-Drive Cryogenic Implosions on OMEGA," to be published in Physics of Plasmas.

24. C. Cerjan, P. T. Springer, and S. M. Sepke, Phys. Plasmas **20**, 056319 (2013).

25. H. S. Bosch and G. M. Hale, Nucl. Fusion **32**, 611 (1992); **33**, 1919(E) (1993).

26. J. J. MacFarlane *et al*., High Energy Density Phys. **3**, 181 (2007).

27. R. Epstein, S. P. Regan, B. A. Hammel, L. J. Suter, H. A. Scott, M. A. Barrios, D. K. Bradley, D. A. Callahan, C. Cerjan, G. W. Collins, S. N. Dixit, T. Döppner, M. J. Edwards, D. R. Farley, K. B. Fournier, S. Glenn,

S. H. Glenzer, I. E. Golovkin, A. Hamza, D. G. Hicks, N. Izumi, O. S. Jones, M. H. Key, J. D. Kilkenny, J. L. Kline, G. A. Kyrala, O. L. Landen, T. Ma, J. J. MacFarlane, A. J. Mackinnon, R. C. Mancini, R. L. McCrory, D. D. Meyerhofer, N. B. Meezan, A. Nikroo, H.-S. Park, P. K. Patel, J. E. Ralph, B. A. Remington, T. C. Sangster, V. A. Smalyuk, P. T. Springer, R. P. J. Town, and J. L. Tucker, AIP Conf. Proc. **1811**, 190004 (2017).

28. F. J. Marshall and J. A. Oertel, Rev. Sci. Instrum. **68**, 735 (1997).

29. H. Brysk, Plasma Phys. **15**, 611 (1973)

30. R. E. Chrien *et al*., Phys. Plasmas **5**, 768 (1998).

31. B. Appelbe and J. Chittenden, Plasma Phys. Control. Fusion **53**, 045002 (2011).

32. T. J. Murphy, Phys. Plasmas **21**, 072701 (2014).

33. *LLE Review Quarterly Report* **150**, 100, Laboratory for Laser Energetics, University of Rochester, Rochester, NY, NTIS Order No. DOE/NA/1944-1331 (2017). Copies may be obtained from the National Technical Information Service, Springfield, VA 22161.

34. B. K. Spears, M. J. Edwards, S. Hatchett, J. Kilkenny, J. Knauer, A. Kritcher, J. Lindl, D. Munro, P. Patel, H. F. Robey, and R. P. J. Town, Phys. Plasmas **21**, 042702 (2014).

35. I. V. Igumenshchev, D. T. Michel, R. C. Shah, E. M. Campbell, R. Epstein, C. J. Forrest, V. Yu. Glebov, V. N. Goncharov, J. P. Knauer, F. J. Marshall, R. L. McCrory, S. P. Regan, T. C. Sangster, C. Stoeckl, A. J. Schmitt, and S. Obenschain, Phys. Plasmas **24**, 056307 (2017).

36. K. M. Woo, R. Betti, Shvarts. D., A. Bose, D. Patel, R. Yan, P.-Y. Chang, O. M. Mannion, R. Epstein, J. A. Delettrez, M. Charissis, K. S. Anderson, P. B. Radha, A. Shvydky, I. V. Igumenshchev, V. Gopalaswamy, A. R. Christopherson, J. Sanz, and H. Aluie, Phys. Plasmas **25**, 052704 (2018).

37. C. Stoeckl, R. Epstein, R. Betti, W. Bittle, J. A. Delettrez, C. J. Forrest, V. Yu. Glebov, V. N. Goncharov, D. R. Harding, I. V. Igumenshchev, D. W. Jacobs-Perkins, R. T. Janezic, J. H. Kelly, T. Z. Kosc, R. L. McCrory, D. T. Michel, C. Mileham, P. W. McKenty, F. J. Marshall, S. F. B. Morse, S. P. Regan, P. B. Radha, B. S. Rice, T. C. Sangster, M. J. Shoup III, W. T. Shmayda, C. Sorce, W. Theobald, J. Ulreich, M. D. Wittman, D. D. Meyerhofer, J. A. Frenje, M. Gatu Johnson, and R. D. Petrasso, Phys. Plasmas **24**, 056304 (2017).

38. R. C. Shah, B. M. Haines, F. J. Wysocki, J. F. Benage, J. A. Fooks, V. Glebov, P. Hakel, M. Hoppe, I. V. Igumenshchev, G. Kagan, R. C. Mancini, F. J. Marshall, D. T. Michel, T. J. Murphy, M. E. Schoff, K. Silverstein, C. Stoeckl, and B. Yaakobi, Phys. Rev. Lett. **118**, 135001 (2017).

39. I. V. Igumenshchev, V. N. Goncharov, F. J. Marshall, J. P. Knauer, E. M. Campbell, C. J. Forrest, D. H. Froula, V. Yu. Glebov, R. L. McCrory, S. P. Regan, T. C. Sangster, S. Skupsky, and C. Stoeckl, Phys. Plasmas **23**, 052702 (2016).

40. D. T. Michel, I. V. Igumenshchev, A. K. Davis, D. H. Edgell, D. H. Froula, D. W. Jacobs-Perkins, V. N. Goncharov, S. P. Regan, A. Shvydky, and E. M. Campbell, Phys. Rev. Lett. **120**, 125001 (2018).

41. R. Betti, A. R. Christopherson, B. K. Spears, R. Nora, A. Bose, J. Howard, K. M. Woo, M. J. Edwards, and J. Sanz, Phys. Rev. Lett. **114**, 255003 (2015).

42. A. R. Christopherson, R. Betti, A. Bose, J. Howard, K. M. Woo, E. M. Campbell, J. Sanz, and B. K. Spears, Phys. Plasmas **25**, 012703 (2018).